Analysis of proton + ^{12}C scattering by microscopic coupled-channels calculations

M. Tomita,[1] M. Iwasaki,[1] R. Otani,[1] K. Horio,[1] and M. Ito[1,2]
[1]*Department of Pure and Applied Physics, Kansai University, Yamatecho 3-3-35, Suita, Japan*
[2]*Research Center for Nuclear Physics (RCNP), Osaka University, Mihogaoka 10-1, Suita 567-0047, Japan*
(Received 30 April 2015; revised manuscript received 3 June 2015; published 11 August 2015)

The microscopic coupled-channel (MCC) calculations for proton + ^{12}C inelastic scattering are performed in the energy range of $E_p = 29.95$ to 65 MeV. The nuclear interactions for the proton-^{12}C system are constructed from the folding model, which employs the internal wave function of ^{12}C, obtained from the 3α resonating group method (3α RGM), and an effective nucleon-nucleon interaction of the density-dependent Michigan three-range Yukawa (DDM3Y). The MCC calculation with the 3α RGM + DDM3Y nicely reproduces all of the differential cross sections for elastic and inelastic scattering in the angular range of $\theta_{\text{c.m.}} = 30$ to 120°. The channel-coupling effect is analyzed by comparing the full MCC calculation with the calculation of the distorted wave Born approximation (DWBA). The effect of the spin-orbit interaction, obtained in a simplified manner with the folding procedure, is also discussed.

DOI: 10.1103/PhysRevC.92.024609 PACS number(s): 21.60.Gx, 24.10.Eq, 25.60.Je

I. INTRODUCTION

Nucleon scattering from carbon is very important in the fields of nuclear engineering [1] and medical technology [2]. For example, a neutron + carbon reaction occurs in nuclear reactors because carbon is often used as the moderator of neutrons to control the nuclear reactions in reactors. The neutron-carbon interaction is very important to correctly evaluate the reaction probability in a moderator. The nucleon-carbon reaction is also related to radiation therapy for humans because carbon is one of the main elements of human tissue. In radiation therapy, cancer cells in human tissue are irradiated by a proton beam and the proton + carbon reaction is important. To understand the nucleon-carbon interaction more precisely, a theoretical analysis of nucleon scattering by a carbon target is needed over a wide range of scattering energy. Since neutron acceleration control is challenging [3], proton scattering has been measured in scattering experiments, and the neutron-carbon interaction is speculated by switching off the Coulomb interaction.

The ^{12}C nucleus has characteristic features, such as the coexistence of different kinds of nuclear structures; specifically, a spatially compact structure and a well-developed 3α structure coexist in this nucleus [4,5]. The ground 0^+_1 state has a spatially compact structure in which all nucleons are tightly bound to each other. The excited states of 2^+_1 at 4.44 MeV and 3^-_1 at 9.64 MeV have similar compact structures, which correspond to the rotational and vibrational excitation of the ground state, respectively. In contrast, the 0^+_2 state at 7.65 MeV has a 3α structure in which the ^{12}C nucleus is decomposed into 3α particles and they are weakly coupled to each other. The 2^+_2 state located at 10.3 MeV is also the 3α state, which is generated by the rotational excitation of the 0^+_2 state [5]. These two kinds of nuclear structures are nicely described by the calculation of the resonating group method (RGM) of the 3α particle, in which an antisymmetrization among a whole nucleon in the 3α particle is fully taken into account [4].

In a theoretical analysis of the proton-carbon reaction, the characteristic feature in ^{12}C, the coexistence of two kinds of nuclear structures should be taken into account. There are many theoretical analyses of proton (p) + ^{12}C elastic scattering [6,7] and inelastic scattering [8–11]. In the analysis of elastic scattering, the differential cross section and analyzing power are calculated on the basis of the optical potential model at 65 MeV $\leqslant E_p \leqslant$ 200 MeV [6,7], whereas the coupled-channel (CC) calculation [9–11] and the method of the distorted wave impulse approximation [8] have been applied to inelastic scattering at the energy of $E_p \leqslant 65$ MeV and $E_p = 200$ MeV, respectively. In the CC calculations in Refs. [9,10], the observed cross sections are nicely reproduced, but the internal state of ^{12}C is treated by a phenomenological collective model in which the coexistence properties of the compact and extended 3α structures in ^{12}C are not explicitly implemented. In contrast, in the calculation in Ref. [11], the proton-carbon interaction is derived from the folding model, which employs the 3α RGM wave function of ^{12}C and an effective nucleon-nucleon (NN) interaction. This CC calculation based on the 3α RGM wave function can nicely reproduce the various data, but the NN interaction is treated in a phenomenological manner. That is, the parameters included in the effective NN interaction are optimized so as to reproduce the observed differential cross sections of the inelastic scattering.

In the present studies, we perform the more sophisticated CC calculation for the p + ^{12}C inelastic scattering, in which the shortcoming of the previous CC calculations [9–11] is improved. Specifically, the nuclear interactions of p + ^{12}C are constructed in the full microscopic manner on the basis of the 3α RGM wave function and the effective NN interaction with a reliable foundation. As for the NN interaction, the Michigan three-range Yukawa (M3Y) interaction [12,13] and its density-dependent version (DDM3Y) [14] are employed. These NN interactions were derived not in a phenomenological manner but from the microscopic calculation of infinite nuclear matter [12]. They are tuned so as to reproduce the scattering phenomena in light ion systems, such as in ^{12}C + ^{12}C, ^{12}C + ^{16}O, and so on [13,14].

The coupled-channel formalism based on the DDM3Y (or M3Y) effective NN interaction and the microscopic internal wave function is called the microscopic

coupled-channel (MCC) calculation [15–20]. The MCC calculations are successful in describing the inelastic scattering of the lighter systems, for example, the ^{12}C+^{12}C [15], $\alpha + {}^{12}$C [16], and ^{3}He $+ {}^{12}$C [17]. Therefore, the extension of MCC to the nucleon-nucleus scattering is interesting in the application of the MCC calculation. In the present calculation, the MCC is applied to the $p + {}^{12}$C scattering at the energy range of $E_p =$ 29.95 to 65 MeV, where the impulse approximation is invalid and the channel-coupling effect becomes prominent.

The preliminary result of our MCC calculation of the $p + {}^{12}$C scattering has already been published in Refs. [23,24]. In Ref. [23], we solved the two-channel problem of elastic and inelastic scattering, going to the 0^+_2 state with a well-developed 3α cluster structure. In the present report, we extend the MCC calculation to the multichannel problem of $p + {}^{12}$C inelastic scattering [24], going to the various inelastic channels, which contains the collective excitations of the 2^+_1 and 3^-_1 states and the 3α excitations of the 0^+_2 and 2^+_2 states. From the results of the MCC calculations, we discuss the validity of the nuclear interactions derived from the microscopic folding procedure.

The organization of this article is as follows. In Sec. II, the framework of the MCC is explained. In Sec. III, the theoretical calculations for the $p + {}^{12}$C elastic and inelastic scatterings are compared with the experiments. The channel-coupling effects are analyzed by comparing the full coupled-channel calculation with the method of the distorted wave Born approximation (DWBA). Based on the result of the MCC calculation, the validity of the folding potential, the spin-orbit potential in particular, is discussed. The final section is devoted to a summary and discussion.

II. FRAMEWORK OF THE MICROSCOPIC COUPLED CHANNEL

A. Coupled-channel equations

We solve a set of the coupled-channel (CC) equations for the proton-^{12}C system, which is given in the symbolic form

$$[T_f(\mathbf{R}) + V_{f,f}(\mathbf{R}) - E_f]\chi_f(\mathbf{R}) = -\sum_{i\neq f} V_{f,i}(\mathbf{R})\chi_i(\mathbf{R}). \quad (1)$$

Here, the subscripts f and i design a channel. $T_f(\mathbf{R})$ represents the kinetic energy of the relative motion of the $p + {}^{12}$C system with a relative coordinate $\mathbf{R}$, while $V_{f,i}(\mathbf{R})$ denotes the coupling potential for the transition from channel i to channel f. The total energy in channel f, E_f, is given by the relation of $E_f = E - \epsilon_f$ with a proton's incident energy E and an internal energy of ^{12}C, ϵ_f. $\chi_f(\mathbf{R})$ is the proton-^{12}C relative wave function for channel f, which should be solved in the CC equation. In the present calculation, we include all discrete-excited states of ^{12}C in addition to its ground 0^+_1 state: the rotational state of 2^+_1 (4.44 MeV), the vibrational 3^-_1 state (9.64 MeV), and the 3α cluster states of 0^+_2 (7.65 MeV) and 2^+_2 (10.3 MeV).

In the pragmatic CC calculation, partial wave expansion with the channel-spin representation is applied to the total wave function, and the radial part of the relative wave function, such as $\chi^J_{(sS_a)IL}(R)$, is solved [21,22]. Here, the radial part of the relative wave function is classified in terms of the proton spin $\mathbf{s}$, the internal spin of ^{12}C, $\mathbf{S}_a$, the channel spin $\mathbf{I}(= \mathbf{s} + \mathbf{S}_a)$, the relative spin $\mathbf{L}$, and the total spin $\mathbf{J}(= \mathbf{I} + \mathbf{L})$. Here the subscript of a represents a suffix used to distinguish the internal state of ^{12}C with the same spin ($S_a = 0^+_1, 0^+_2$, and so on). A set of the quantum numbers of $(sS_a)I$ is a channel, while that of $(sS_a)ILJ$ is usually called the subchannel. In the CC calculation, the off-diagonal transition between the subchannels, $(sS_a)ILJ \rightarrow (s'S'_{a'})I'L'J$, is possible according to angular momentum algebra, and this off-diagonal transition corresponds to the channel-coupling effect.

The channel-coupling effect can be classified into two kinds of the transition scheme. One is the transition involving the change of the internal state of ^{12}C, for example, ^{12}C($S_a = 0^+_1 \rightarrow 2^+_1$). This transition is called *dynamical coupling*. The other is a special transition, in which only L is changed and internal state of ^{12}C is invariant; $(sS_a)ILJ \rightarrow (sS_a)IL'J$ [18–20]. This L transition is called *reorientation coupling*. If the proton spin s is neglected, this reorientation coupling corresponds to a transition of the alignment of S_a (internal spin of ^{12}C) with respect to the direction of the total spin J. If the reorientation coupling occurs, the relative spin L can be changed in the range of $L = |J - S_a|$ to $L = J + S_a$ according to angular momentum algebra. There is no reorientation coupling in the spinless state of ^{12}C ($S_a = 0^+_1$ and 0^+_2) but the reorientation effect always appears in the diagonal transition of a finite spin state, such as $2^+_1 \rightarrow 2^+_1$. The reorientation coupling is induced by a component of the nonspherical part (multipole component) in the density distribution. Thus, the reorientation coupling effect becomes prominent if the excited states have a large spin with strong deformation [19,20].

B. Central part in the nuclear potential

The coupling potential ($V_{f,i}(\mathbf{R})$) has a component of the nuclear (N) and Coulomb (C) parts, such as

$$V_{f,i}(\mathbf{R}) = V^{(N)}_{f,i}(\mathbf{R}) + V^{(C)}_{f,i}(\mathbf{R}). \quad (2)$$

The nuclear potential is composed of the real ($V_{f,i}(\mathbf{R})$) and phenomenological imaginary potentials ($-iU_f(R)$),

$$V^{(N)}_{f,i}(\mathbf{R}) = \tilde{V}_{f,i}(\mathbf{R}) - iU_f(R)\delta_{f,i}. \quad (3)$$

The real part of the nuclear potential ($\tilde{V}_{f,i}(\mathbf{R})$) is calculated by the folding model [13,14,18–20], which is expressed symbolically as

$$\tilde{V}_{f,i}(\mathbf{R}) = \int \rho_{f,i}(\mathbf{r}) v^{DDM3Y}_{NN}(|\mathbf{r} - \mathbf{R}|)d\mathbf{r}, \quad (4)$$

where $\mathbf{r}$ denotes the coordinate measured from the center of the mass in the ^{12}C nucleus. Here, $\rho_{f,i}(\mathbf{r})$ represents the diagonal ($f = i$) or transition ($f \neq i$) densities of ^{12}C and is calculated by the resonating group method (RGM) [4] of the 3α cluster model. In Eq. (4), v_{NN} represents the effective nucleon-nucleon (NN) interaction, which acts between a nucleon contained in ^{12}C and an incident proton. The Coulomb interaction in Eq. (2) is calculated by assuming the uniform charge potential with a radius of $R_C = 1.2A^{1/3}$ (fm), and no Coulomb coupling is included in the off-diagonal transition.

In the present work, the density-dependent Michigan three-range Yukawa (DDM3Y) is used for the effective NN interaction. The explicit form of the DDM3Y interaction is given by

$$v_{NN}^{DDM3Y}(s) = \gamma(1 + \alpha e^{-\beta\rho(s)})v_{NN}^{M3Y}(s), \quad (5)$$

with the M3Y interaction of

$$v_{NN}^{M3Y}(s) = 7999\frac{e^{-4s}}{4s} - 2134\frac{e^{-2.5s}}{2.5s} - J_0\delta(\mathbf{s}). \quad (6)$$

In Eq. (5), the parameters of α, β, and γ depend on incident energy per nucleon [14]. Equation (6) corresponds to the NN interaction for the spin (S) and isospin (T) singlet channel ($S = T = 0$). Thus, there is no contribution from the long-range attractive potential generated by the one-pion exchanges. The third term simulates the single-nucleon knock-on exchange with the energy-independent strength of $J_0 = -262$ MeV fm^3 [13]. In the present CC calculation, no modification is done for the folding potentials, although a normalization factor is often introduced in the folding potential for the nucleus-nucleus scattering [17].

The second term in Eq. (3) represents the imaginary potential, which is included only in the diagonal transition ($f = i$). The imaginary potential is composed of two parts, such as

$$U_f(R) = W_{Vf}(R) + W_{Sf}(R). \quad (7)$$

Here, $W_{Vf}(R)$ and $W_{Sf}(R)$ are the Woods-Saxon (WS) potential with volume-type and surface-type form factors, respectively [7,28]. Three parameters, such as strength (W_{0f}), radius (R_f), and diffuseness (a_f), are included in each of the WS potentials. These six parameters are channel dependent, and they are optimized so as to reproduce the observed differential cross sections as much as possible. In the present calculation, we neglect the imaginary potentials in the off-diagonal transition for simplicity. All the parameters used in the present MCC calculation are listed in the Appendix (Tables I–IV).

Let us discuss the physical origin of the volume and surface imaginary potentials introduced in the present calculation. The volume parts mainly simulate the absorption of the incident proton, and this absorption leads to the formation of the compound system of ^{13}C and the complicated process inside of the compound states. On the other hand, one of the main reaction process that is simulated by the surface-type absorption is the coupling to transfer channels, such as the pickup reaction, ^{12}C$(p,d)^{11}$C [25,26], for example. In the previous experiments at $E_p = 51.9$ MeV [26], the angular distribution of ^{12}C$(p,d)^{11}$C$(3/2^-)$ was measured, and the distribution was compared with the cross section of the inelastic scattering to the 2_1^+ channel. The magnitude of the cross section of the pickup reaction is almost the same as the cross section of the inelastic scattering ($\sim$10 mb/sr). Furthermore, the angular distribution of the pickup reaction strongly suggests the nonzero orbital spin transfer ($\Delta L \neq 0$), which can be confirmed by the rapid decrease of the cross section at the forward angle, $\theta_{\rm c.m.} \sim 0^\circ$. These results of ^{12}C$(p,d)^{11}$C means that the pickup process, which competes with the inelastic scattering, mainly occurs at the surface region of the nuclear potential. Therefore, the introduction of the surface-type absorption is considered to be valid in order to simulate the pickup reaction.

C. Spin-orbit interaction

In the calculation of the scattering to the spinless channels, the 0_1^+ and 0_2^+ channels, we include the spherical spin-orbit interaction, such as

$$\tilde{V}_{f,i}(\mathbf{R}) \rightarrow \tilde{V}_{f,i}(\mathbf{R}) + V_{f,i}^{LS}(R)\mathbf{L}\cdot\mathbf{s}. \quad (8)$$

The radial form factor of the spin-orbit potential, $V_{f,i}^{LS}(R)$, is calculated according to the simplified folding procedure

$$V_{f,i}^{LS}(R) = -\frac{\pi}{2}\frac{1}{R}\frac{\partial\rho_{f,i}^{\rm mono}(R)}{\partial R}\int v_{TO}^{M3Y}(s)s^4 ds, \quad (9)$$

where $v_{TO}^{M3Y}(s)$ represents the triplet-odd (TO) part of the M3Y spin-orbit interaction. The explicit form of TO spin-orbit interaction [12] is

$$v_{TO}^{M3Y}(s) = -3733\frac{e^{-4s}}{4s} - 427.3\frac{e^{-2.5s}}{2.5s}. \quad (10)$$

The M3Y interaction implemented in both the central and spin-orbit interactions is called the Reid version [12,14].

In the derivation of Eq. (9), the short-range property of the spin-orbit NN interaction and cancellation of the triplet-even part and knock-on exchange are assumed [27]. In Eq. (9), the $\rho_{f,i}^{\rm mono}(R)$ denotes the monopole transition density, which is the spherical component of the multipole decomposition in the transition density [4,19]. The folding potential in Eq. (9) was originally derived for the nucleon scattering by a spherical and a spinless target [27]. Equation (9) is very useful because the spin-orbit potential is easily obtained from the simple derivative of the monopole transition density. In the present CC calculation, the folding potential in Eq. (9) is extended in a straightforward manner; specifically, the internal spin of all the excited states in the ^{12}C nucleus is neglected, and the spin-orbit couplings are included in the monopole transitions between the same spin states, such as the $0_1^+ \rightarrow 0_2^+, 2_1^+ \rightarrow 2_2^+, 3_1^- \rightarrow 3_1^-$, and so on. We investigate the validity of the simple prescription of the spin-orbit potential in Eq. (9).

III. RESULTS

A. Systematic calculation of the differential cross sections

We show the results of the full CC calculation with the nuclear interaction in Eqs. (3) and (4). In this calculation, all the spin-orbit interactions are switched off, and the proton is treated as the spinless particle ($s = 0$). Figures 1, 2, 3, and 4 show the results of the differential cross sections, going to the 0_1^+, 2_1^+, 3_1^-, and 0_2^+ channels, respectively. The comparison of the CC calculations (solid curves) with the experiments (asterisks) are done in the energy range of $E_p = 29.95$ to 65 MeV.

The CC calculations for the elastic (0_1^+) and 2_1^+ channels, which are shown in Figs. 1 and 2, respectively, nicely reproduce the overall features of the observed differential cross sections except for the backward angles of $\theta_{\rm c.m.} \geqslant 120^\circ$ at the energies of $E_p \leqslant 39.95$ MeV. In the MCC calculation of the 0_1^+ channel, a prominent valley appears at the angle

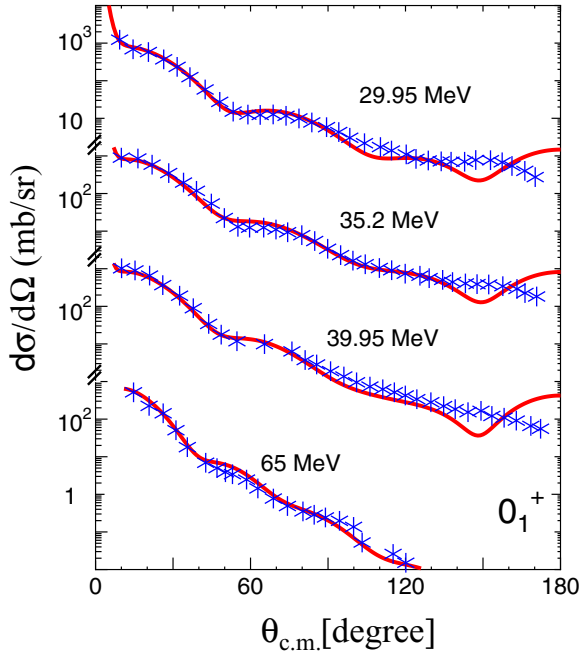

FIG. 1. (Color online) Differential cross section of the elastic(0_1^+) scattering in the range of $E_{\rm lab} = 29.95$ to 65 MeV. The asterisks and the curves represent the experimental data and the theoretical calculations, respectively.

of $\theta_{\rm c.m.} = 130^\circ$, and the calculated cross section quickly increased beyond 130° in comparison to the experimental data. Such valley-peak structures in the theoretical calculation are observed in the 2_1^+ channel (Fig. 2), and the CC calculation is out of phase at $\theta_{\rm c.m.} = 130^\circ$. The valley-peak structures at the backward angles were also observed in the previous CC calculation based on the soft-rotator model [9].

The present CC calculation nicely reproduces the cross section going to the 3_1^- state, especially in the angular range of $30^\circ \leqslant \theta_{\rm c.m.} \leqslant 140^\circ$, as shown in Fig. 3. At $E_p = 35.2$ and 39.95 MeV, the valley-peak structures, which are confirmed in the 2_1^+ channel, also appear around $\theta_{\rm c.m.} \sim 150^\circ$. In addition,

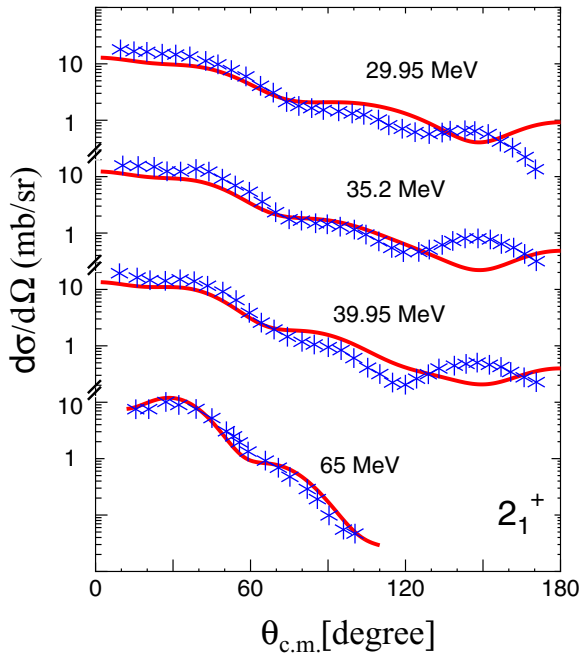

FIG. 2. (Color online) Same as Fig. 1 except for the inelastic 2_1^+ channel.

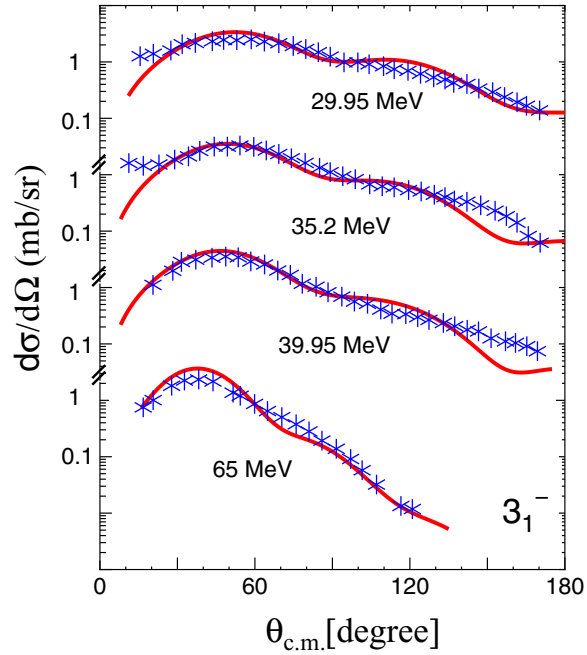

FIG. 3. (Color online) Same as Fig. 1 except for the inelastic 3_1^- channel.

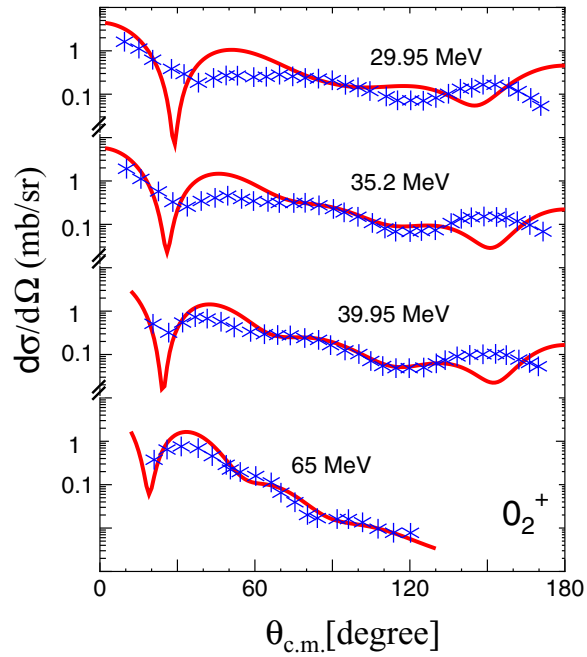

FIG. 4. (Color online) Same as Fig. 1 except for the inelastic 0_2^+ channel.

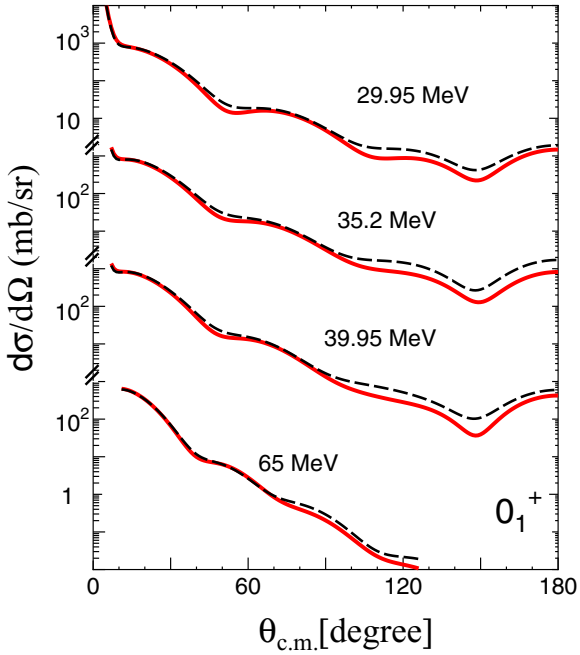

FIG. 5. (Color online) Comparison of the full CC calculations with the DWBA calculations in the elastic channel. The solid curve shows the result of the full CC calculations, while the dashed curves represent the DWBA calculations.

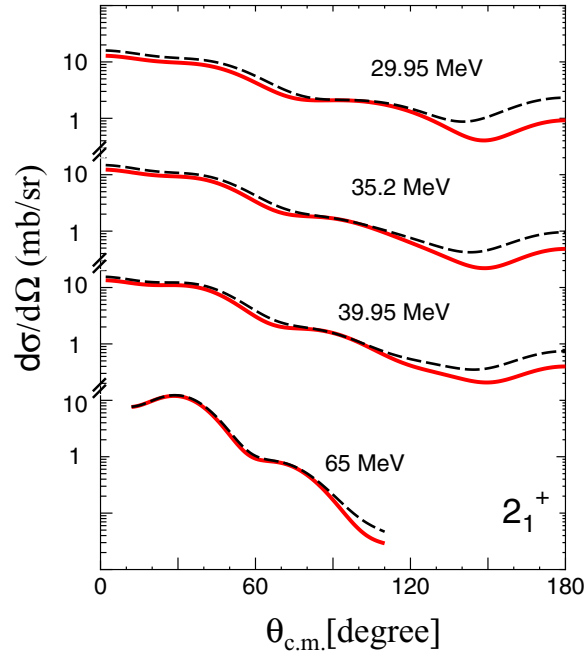

FIG. 6. (Color online) Same as Fig. 5 except for the inelastic 2_1^+ channel.

the CC calculations underestimate the cross sections at the forward angles of $\theta_{\text{c.m.}} \leqslant 20^\circ$ at the lower energy region, $E_p = 29.95$ and 35.2 MeV.

The results of the CC calculation for the 0_2^+ state, which has the well-developed three α structures, are shown in Fig. 4. In all the energy ranges, the theoretical calculations reasonably reproduce the global features of the observed cross sections. However, the deviations of the CC calculation from the experimental data are more prominent in comparison to other collective channels, such as the 0_1^+, 2_1^+, and 3_1^+ channels. At the backward angles of $\theta_{\text{c.m.}} \sim 150^\circ$ the CC calculation is out of phase in comparison to the experimental data. Being out of phase is a common feature in all the inelastic channels. Moreover, a sharp valley appears in the CC calculation at the angle of $\theta_{\text{c.m.}} = 30^\circ$, and this valley is largely deviated from the observed data except for the incident energy of $E_p = 65$ MeV.

The present CC calculations are successful in reproducing the differential cross section in the angular range of $\theta_{\text{c.m.}} = 30$–$120^\circ$, although the fit to the experimental data depends considerably on the exit channels. There is a common feature in the deviation between the theory and the experiment: the out-of-phase structure at the backward angle of $\theta_{\text{c.m.}} \geqslant 130^\circ$. In the 0_2^+ and 3_1^- channels, moreover, the deviation of the CC calculation from the experiments is confirmed at the forward angular region.

B. Analysis of the channel coupling effect

We discuss multistep coupling in the reaction process. Figures 5, 6, 7, and 8 represent comparisons of the full CC calculation and the calculation of the DWBA [21,22]. The former and latter results are shown by the solid and dotted curves, respectively, in the individual figures. In both the CC and DWBA calculations, the spin-orbit interaction is switched off and the proton spin is set to $s = 0$.

In the DWBA calculation, all the off-diagonal transitions from the ground subchannel, which are represented by

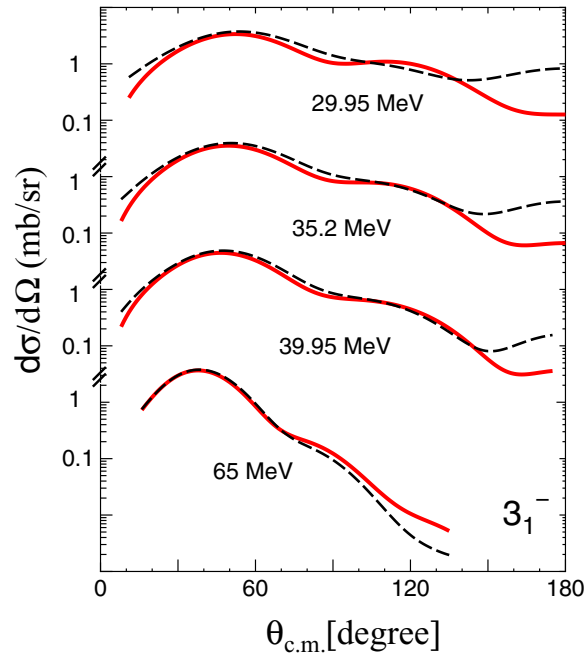

FIG. 7. (Color online) Same as Fig. 5 except for the inelastic 3_1^- channel.

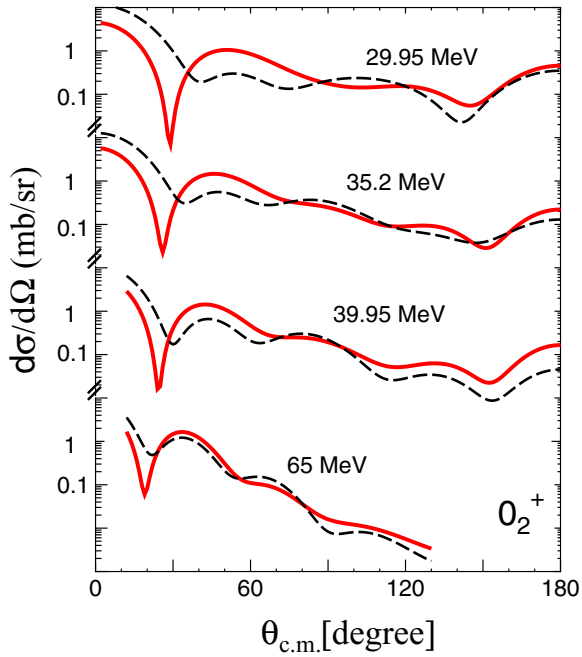

FIG. 8. (Color online) Same as Fig. 5 except for the inelastic 0_2^+ channel.

$(S_a, L = J, J) = (0_1^+, J, J) \rightarrow (S'_{a'}, L', J)$ with $S'_{a'} = 0_2^+$, 2_1^+, and 3_1^- are treated in the first-order perturbation, while the couplings among the excited subchannels, $(S'_{a'}, L', J) \rightarrow (S''_{a''}, L'', J)$, are switched off. Therefore, in the DWBA, the coupling of the ground 0_1^+ channel to all the excited channels terminates in the one-step transition. In contrast, the infinite multistep transitions among the channels are fully taken into account in the full CC calculation. If the channel coupling effect is weak, the DWBA calculation gives the same results as the CC calculation.

In the result of the 0_1^+ channel (Fig. 5), the DWBA results are almost indistinguishable from the CC results in the forward angles of $\theta_{\text{c.m.}} \leqslant 90^\circ$. However, the difference of the full CC and DWBA is prominent at the backward region, such as $\theta_{\text{c.m.}} \geqslant 90^\circ$, in the lower energy region of $E_p \leqslant 39.95$ MeV. This result means that multistep coupling is important in the backward scattering. The strong effect of the multistep coupling at the backward angle is naturally expected from a general feature of the channel-coupling effect. The backward scattering occurs when the incident proton wave deeply penetrates the inside region of the ^{12}C nucleus. Thus, the proton scattered at the backward angle strongly feels the nuclear field of the ^{12}C target, and the multistep effect by the nuclear interaction becomes prominent. In contrast to the lower energy region, the CC calculation is almost the same as the DWBA calculation at the higher incident energy, $E_p =$ 65 MeV. This is because the interaction time becomes short in the higher energy scattering; hence, the multistep coupling becomes weak.

In the result of the 2_1^+ channel (Fig. 6), a similar feature to the 0_1^+ channel is seen. Specifically, the difference of CC (solid curves) and DWBA (dashed curves) is prominent at the backward angles in the lower energy region ($E_p \leqslant 39.95$ MeV), but the CC effect is less important in the high energy region ($E_p = 65$ MeV). The difference of CC and DWBA at the backward scattering is common to the 0_1^+ and 2_1^+ channels. Since the 0_1^+ and 2_1^+ states form the ground rotational band [4], the coupling of these two channels is strong [18]. Thus, the backward difference of DWBA and CC is attributed to the multistep effect of the dynamical coupling of $0_1^+ \rightarrow 2_1^+$.

In the forward angles of $\theta_{\text{c.m.}} \leqslant 90^\circ$ at $E_p \leqslant 39.95$ MeV, the DWBA results closely follow the CC results, but the DWBA results slightly deviate from the CC results. In the forward scattering, the dynamical coupling of $0_1^+ \rightarrow 2_1^+$ is expected to be small. Since there is a reorientation coupling in the 2_1^+ channel, which does not exist in the spinless 0_1^+ channel, the origin of the deviation at the forward angle is considered to be the reorientation coupling, which arises from the diagonal transition of $2_1^+ \rightarrow 2_1^+$ in the final channel.

The comparison of CC with DWBA for the 3_1^- channel is shown in Fig. 7. The differences in these two calculations are prominent at the backward angles, and this feature is similar to the results of the 0_1^+ and 2_1^+ channels, which are confirmed in Figs. 5 and 6, respectively. The backward difference is generated by the multistep effect of the dynamical coupling of $0_1^+ \rightarrow 3_1^+$, because the 0_1^+ and 3_1^+ states have a common nuclear structure. This coupling gives a considerable effect at the backward scattering, although its effect is weaker than the coupling of $0_1^+ \rightarrow 2_1^+$ [18].

In the forward scattering at $\theta_{\text{c.m.}} \leqslant 90^\circ$, we can confirm that the DWBA results deviate considerably from the CC results, and this deviation is more prominent than the deviation in the 2_1^+ channel (Fig. 6). Since the intrinsic deformation in the 3_1^- state is stronger than that in the 2_1^+ state [4], the reorientation coupling among the subchannels with the 3_1^- state is enhanced more than the reorientation among the 2_1^+ subchannels. The enhanced reorientation coupling especially affects on the forward scattering. In fact, we can see the clear difference of DWBA and CC at the extremely forward angle of $\theta_{\text{c.m.}} \leqslant 30^\circ$.

In contrast to the 0_1^+, 2_1^+, and 3_1^- channels, there is the large difference of CC and DWBA in the 0_2^+ channel, as shown in Fig. 8. In the forward region, the angular distribution calculated by DWBA (dashed curves) has a strong oscillating structure in comparison to the CC calculation (solid curves). Moreover, the magnitude of the cross section in the full CC calculation is reduced in comparison to the magnitude of the DWBA calculation. This reduction in the full CC suggests that the flux in the 0_2^+ channel is strongly absorbed to another channel by the multistep coupling.

The origin of the absorption is not the reorientation coupling but the dynamical coupling because the 0_2^+ channel is a spinless state. The 0_2^+ state has a well-developed 3α cluster structure with a spatial extension, and hence this state can easily be excited to its rotational excited state of the 2_2^+ state [4]. Therefore, the difference of DWBA and CC originates from the coupling of $0_2^+ \rightarrow 2_2^+$. The inclusion of the 2_2^+ state is essential in the calculation of the inelastic scattering to the 0_2^+ channel.

We perform the restricted CC calculation, in which the coupling to 2_2^+ is switched off, to investigate the effect of the coupling to the 2_2^+ channel more clearly. In Fig. 9, the results of the restricted CC calculation are compared to the

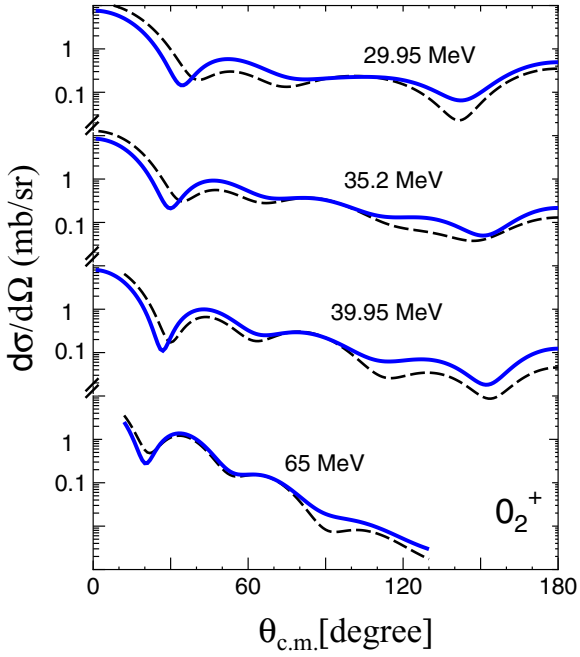

FIG. 9. (Color online) Comparison of the restricted CC calculation without 2_2^+ and the DWBA calculations in the inelastic scattering to the 0_2^+ channel. The solid curve represent the results of the restricted CC calculation without the channel coupling to the 2_2^+ channel, while the DWBA results are plotted by the dashed curves. The DWBA results are the same as the dashed curves shown in the Fig. 8.

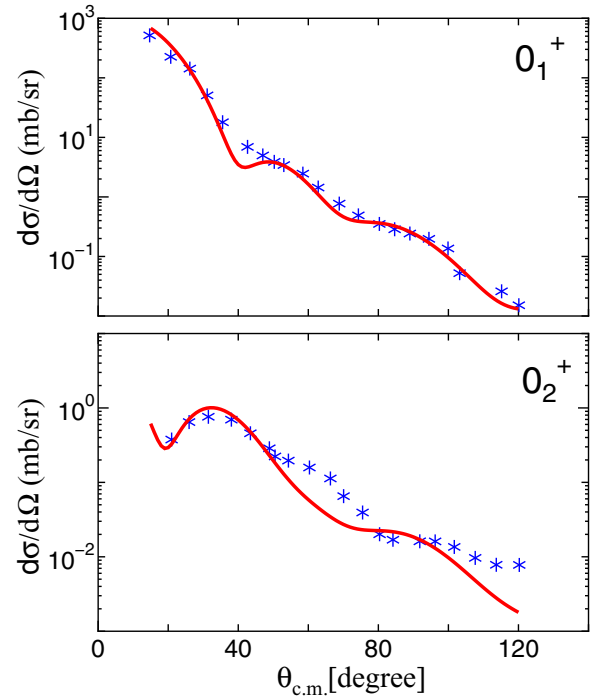

FIG. 10. (Color online) Differential cross section at $E_p =$ 65 MeV in the 0_1^+ and 0_2^+ channels. The asterisk and curve represent the theoretical calculations, respectively.

DWBA calculation. The restricted CC calculations without 2_2^+ (solid curves) are nearly same as the DWBA results (dashed curve) although there is a difference in the detailed structure of the angular distributions. This result means that the DWBA calculation is nicely simulated by the restricted CC calculation. Thus, the large deviation of the full CC (solid curves) and DWBA (dashed curves) calculations can be attributed to the coupling effect to the 2_2^+ state. This result is consistent with the analysis of the dynamic polarization potential in the ^{12}C + ^{12}C system at the molecular resonance energy region [18].

C. Effect of the spin-orbit interaction

We discuss the effect of spin-orbit interaction on the elastic and inelastic scattering to the 0_2^+ state. Here we focus on the scattering at $E_p = 65$ MeV because the spin-orbit interaction becomes effective in the higher energy region. In the following calculation, the coupling of the proton spin is treated precisely ($s = 1/2$).

Figure 10 shows the comparison of the theoretical CC calculation (solid curve) with the experimental data (asterisks). In this calculation, no modification of the folding potential is done, and the parameters in the imaginary potentials are optimized so as to reproduce both angular distributions. The observed cross section of the elastic (0_1^+) scattering is nicely reproduced although the dip of the solid curve at $\theta_{\text{c.m.}} = 40^\circ$ seems to be steeper than the experimental observation. On the contrary, the reproduction of the inelastic scattering to the 0_2^+ channel is not greatly improved. In this inelastic scattering, a steep dip around $\theta_{\text{c.m.}} = 30^\circ$, which is observed in Fig. 4, becomes a moderate dip, leading to a good fit to the observation at the forward angle. However, the oscillation pattern of the calculation is out of phase at the backward angle in comparison to the experiments. We tried to search the imaginary potentials to reproduce the cross section over a whole angle, but the reproduction of the observed phase was difficult.

We change the potential to obtain a better fit to the experiments in the following step. First, we include the spin-orbit potential only in the diagonal transition of the 0_1^+ channel, and all other spin-orbit potentials for the monopole transitions are switched off. Second, we search the parameters of the imaginary potential in this modified treatment of the spin-orbit potential. Figure 11 represents the result of the modified calculation. We can clearly confirm that the modified calculation nicely reproduces the global features of the oscillating pattern in the differential cross section. In the elastic channel, the steep dip at $\theta_{\text{c.m.}} = 40^\circ$ disappears, and the fit to the experiment is improved. As for the 0_2^+ channel, the oscillating phase in the modified calculation reproduces the observed phase over a whole angle although the theoretical calculation still overestimates the magnitude of the cross section at $\theta_{\text{c.m.}} = 30^\circ$.

The theoretical calculations shown in Figs. 10 and 11 suggest that the spin-orbit potential calculated from Eq. (9) is inappropriate for describing a realistic inelastic scattering. The functional form in Eq. (9) has been derived for the elastic scattering by the spinless target [27], but its validity is unclear, especially in the treatment of the inelastic scattering induced by the off-diagonal transition density. Thus, a more precise

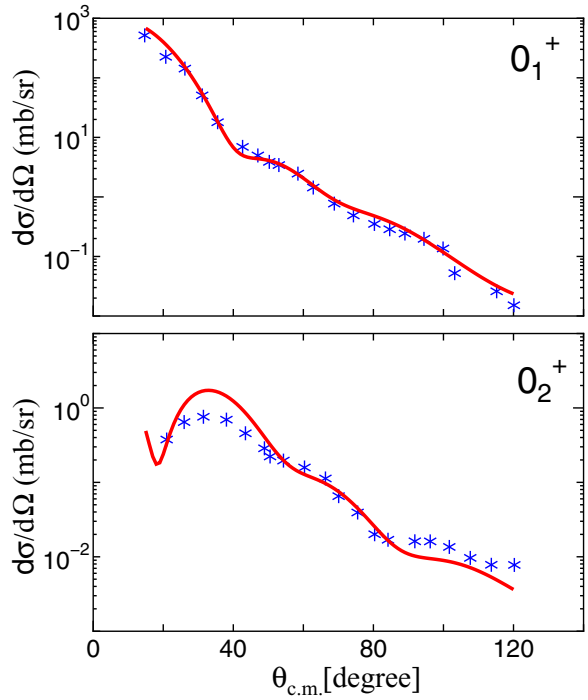

FIG. 11. (Color online) The same as Fig. 10 except for the calculation with the modified treatment of the spin-orbit potentials. See text for details.

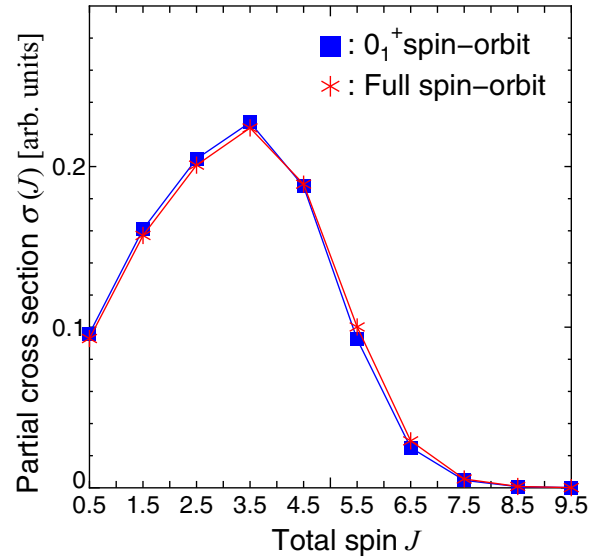

FIG. 12. (Color online) Distributions of the partial cross sections for the elastic at $E_p = 65$ MeV. The asterisks show the results of the calculation with the full spin-orbit potential, while the solid squares represent the results with the restricted spin-orbit potential. See text for details.

treatment of the folding potential should be considered for the spin-orbit coupling in the coupled-channel formalism.

To investigate the effect of the spin-orbit potential in greater depth, we analyze the distribution of the partial cross sections, $\sigma(JL)$, which represents the decomposition of the angle-integrated cross section into the individual contributions of the partial waves, which are classified by the total (J) and relative (L) spins. As pointed out in our recent study [23], the partial cross section is an important quantity to characterize a size of the reaction area although the partial cross sections themselves are not direct observables. The partial cross sections of the elastic 0_1^+ channel are shown in Fig. 12. In this figure, the partial cross sections with different L belonging to a common J is summed up as $\sigma(J) = \sum_L \sigma(JL)$, and they are normalized by the total cross section of $\sigma = \sum_J \sigma(J)$. In the partial cross section plotted in Fig. 12, the contribution from the Coulomb scattering is excluded; hence, the plotted partial cross sections are converged to finite values.

In Fig. 12, the partial cross sections with the full spin-orbit potential are shown by the asterisks, while those with the restricted spin-orbit potential, in which the spin-orbit potential is included only in the diagonal transition of the ground 0_1^+ channel, are shown by the solid square. Since the asterisks are almost indistinguishable from the solid squares, the effect of the off-diagonal coupling in the spin-orbit potential is weak for the elastic channel. Thus, the elastic scattering is dominated by the diagonal spin-orbit potential in this channel.

In contrast, we can confirm the strong effect of the spin-orbit potential in inelastic scattering, going to the 0_2^+ channel. In Fig. 13, the partial cross sections for the 0_2^+ channel are shown.

The symbols in Fig. 13 are the same as those in Fig. 12. As can clearly be seen in Fig. 13, $\sigma(J)$ with the full spin-orbit (asterisks) has a more extended distribution in comparison to the results with the restricted spin-orbit potential (solid squares). This result means that the spin-orbit potential causes the inelastic scattering of the higher partial waves, and the higher partial wave contribution generates an unrealistic oscillation in the angular distribution, as shown in the lower panel of Fig. 10.

In the inelastic scattering to the 0_2^+ channel, there are two kinds of dominant spin-orbit couplings: the off-diagonal coupling of $0_1^+ \to 0_2^+$ and the diagonal coupling of $0_2^+ \to 0_2^+$.

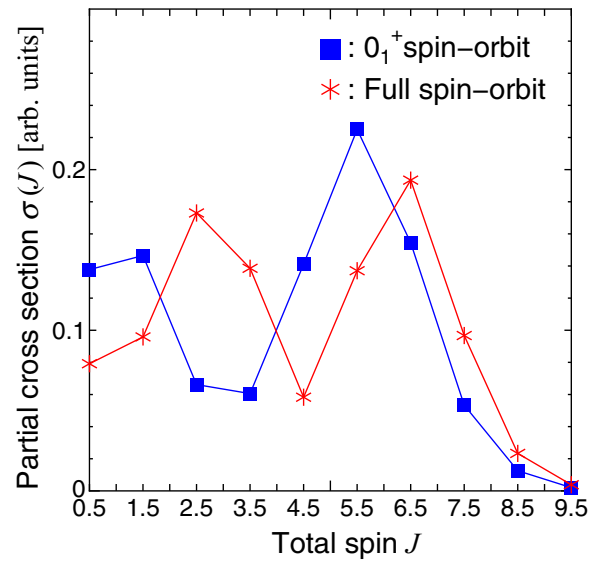

FIG. 13. (Color online) The same as Fig. 12 except for the inelastic channels of the 0_2^+ state.

We have confirmed that the former coupling is dominant. Therefore, the off-diagonal spin-orbit potential should be improved by more sophisticated treatment than the simple formula according to Eq. (9).

IV. SUMMARY AND DISCUSSION

In sum, we have performed the microscopic coupled-channel (MCC) calculation in the proton + ^{12}C scattering in the energy range of $E_p = 29.95$ to 65 MeV. In the framework of MCC, the real part of the nuclear potentials are derived from the precise wave function of ^{12}C, which are calculated by the 3α resonating group method (3α RGM), and the reliable nucleon-nucleon (NN) interaction, such as the density-dependent Michigan 3-range Yukawa (DDM3Y) and the Michigan three-range Yukawa (M3Y). In addition to the real potential, we have introduced an imaginary potential with the form factor of the Woods-Saxon potential for the diagonal coupling, and the parameters in the imaginary potentials are optimized to reproduce the differential cross sections.

The MCC calculation with 3α RGM + DDM3Y can nicely reproduce the observed angular distributions in the angular region of $\theta_{\text{c.m.}} = 30$ to 120°. The fit to the experimental data in the present MCC calculation is superior to the previous coupled-channel calculations that were based on the phenomenological treatment in the coupling potential [9–11]. Reproduction of the experiments by the microscopically derived nuclear interactions is an important development in the theoretical calculations. However, the reproduction of the detailed structures is still insufficient especially in the backward ($\theta_{\text{c.m.}} \geqslant 120^\circ$) and forward scattering ($\theta_{\text{c.m.}} \leqslant 30^\circ$). In the backward scattering, the theoretical calculations for all the exit channels commonly generate the valley-peak structures, which are out of phase in the oscillating pattern of the angular distribution by comparing the experimental data. Since the proton scattered to the backward angle strongly feels the interior density of the ^{12}C target, the modification of the interior part of the transition density may be important for the improvement of the fit to the backward scattering.

On the contrary, the failure of the forward scattering is confirmed only in the 3^-_1 and 0^+_2 channels, which are the unbound resonant states above the 3α threshold [4]. Thus, the failure of the forward scattering seems to relate to the resonant property of these two states. In the unbound resonances, the tail part of the density is extended to a wide spatial region due to the quantum tunneling effect. Since the forward scattering is sensitive to the tail part of the transition density, the precise treatment of the tail is especially important in the treatment of the scattering to the resonant states. Therefore, the possibility exists that the careful treatment of the tail part in the resonant density may lead to an improvement in the reproduction of the experimental data.

The channel coupling effect is analyzed by performing the DWBA. In comparison with the DWBA and the full CC calculations, the channel-coupling effect is confirmed, especially in the backward scattering in the 0^+_1, 2^+_1, and 3^-_1 channels. In the 2^+_1 and 3^-_1 channels, there is the extra effect of the channel coupling in the forward scattering. The coupling at the forward angle is considered to be the effect of the reorientation coupling, which is peculiar to the excited states with a finite spin. The channel coupling effect for the 0^+_2 channel, which has the well-developed 3α structure, is the most prominent of all the channels. The origin of this effect is the coupling to the 3α rotational state, the 2^+_2 state.

We have also investigated the effect of the spin-orbit potential on the spinless exit channels, 0^+_1 and 0^+_2. The radial form of the spin-orbit potential is obtained from a simple derivative form of the transition density with the density-independent NN interaction, M3Y. The inclusion of the spin-orbit potential partially improves the forward scattering in the 0^+_2 channel, but the CC calculation with the spin-orbit interaction fails to reproduce the global behavior of the oscillation pattern in the differential cross section. We have obtained a better fit by switching off the spin-orbit potential except for the diagonal transition in the elastic channel.

The effect of the spin-orbit potential is also investigated by the analysis of the partial cross section. The off-diagonal transition induced by the spin-orbit potential has a minor effect on the elastic scattering, but its effect is prominent in the 0^+_2 channel. The inclusion of the spin-orbit transition induces the scattering of the higher partial waves, which leads to unrealistic oscillation in the angular distribution. The result of the present analysis strongly suggests that the simplified folding procedure with density-independent NN spin-orbit interaction should be reconsidered especially for the excited channel although the central part of the folding potential is considered to be a realistic interaction.

In the present study, we have focused on proton scattering, but we should extend the MCC calculation to neutron scattering as well, which is obtained in the energy region of $E_n \leqslant 40.3$ MeV [9,28]. The MCC calculation for the low-energy neutron scattering is important in the compilation of nuclear data in nuclear engineering and medical technology. Moreover, deep analysis of the partial cross section should be done for the present multichannel problem. As pointed out in Ref. [23,24], the distribution of the partial cross sections is useful in defining a size of the spatial area, where the final channels are produced. The radii evaluated from the partial cross sections, which are called the "scattering radii" [23,24], may have a close connection to the matter radius of the excited states, which is impossible to measure directly in experiments. Systematic calculations of neutron scattering and the analysis of the scattering radius are currently under way.

ACKNOWLEDGMENTS

The authors thank Prof. A. Kohama for his valuable comments and encouragement. We also thank Prof. Y. Iseri for his tutorial support of the computational program. One of the authors (M.I.) also thanks Prof. Chiba for providing the experimental information and his useful comments. This work has been supported by a Grant-in-Aid for Scientific Research in Japan (No. 26400284).

APPENDIX

In this Appendix, the parameter sets of the imaginary potentials included in the diagonal transition, shown in

TABLE I. Incident energy dependence of the parameter sets for the elastic (0_1^+) channel. At the left-most column, the proton incident energy is shown, and the parameters of the volume type (W_{0V}, R_V, and a_V) and surface type (W_{0V}, R_V, and a_V) are listed for the individual energies.

Energy	W_{0V}	R_V	a_V	W_{0S}	R_S	a_S
29.95	6.5	3.0	0.6	3.0	0.5	0.6
35.2	5.2	1.5	0.6	4.6	1.7	0.6
39.95	3.5	2.2	0.6	4.5	2.0	0.6
65	6.8	1.5	0.6	17.9	1.43	0.6

Eq. (7), are listed. In all the channels, the imaginary potential comprises the Woods-Saxon potential with the volume (V) and surface (S) form factors. In each of the Wood-Saxon potential, there are three parameters, such as the depth (W_0), radius (R), and the diffuseness (a) parameters. The parameters listed in the following are employed the MCC calculation without the spin-orbit potential.

TABLE II. Same as Table I, except for the 2_1^+ channel.

Energy	W_{0V}	R_V	a_V	W_{0S}	R_S	a_S
29.95	2.0	3.0	0.6	3.0	5.0	0.8
35.2	2.5	5.0	0.6	3.0	9.0	0.8
39.95	4.0	2.5	0.6	4.0	5.2	0.6
65	3.0	3.0	0.3	1.0	3.5	0.6

TABLE III. Same as Table I, except for the 3_1^- channel.

Energy	W_{0V}	R_V	a_V	W_{0S}	R_S	a_S
29.95	3.0	3.0	0.6	1.0	2.5	0.6
35.2	3.0	2.5	0.6	2.0	8.5	0.6
39.95	2.0	1.8	0.6	2.0	1.5	0.6
65	0.5	1.0	0.6	0.5	5.7	0.6

TABLE IV. Same as Table I, except for the 0_2^+ and 2_2^+ channels.

Energy	W_{0V}	R_V	a_V	W_{0S}	R_S	a_S
29.95	5.0	2.0	0.6	4.0	5.5	0.6
35.2	4.0	3.8	0.6	3.0	4.0	0.6
39.95	10.0	2.6	0.6	8.0	2.7	0.6
65	2.0	3.0	0.8	2.0	2.0	0.8

[1] M. B. Chadwick, P. G. Yound *et al.*, Nucl. Sci. and Eng. **131**, 293 (1999).
[2] M. B. Chadwick, P. M. DeLcua Jr., and R. C. Haight, Rad. Protect. Dos. **70**, 1 (1997).
[3] Y. Arimoto, P. Gertenbort, S. Imajo, Y. Iwashita, M. Kitaguchi, Y. Seki, H. M. Shimizu, and T. Yoshioka, Phys. Rev. A **86**, 023843 (2012).
[4] Y. Fukushima and M. Kamimura, J. Phys. Soc. Jpn. **44**, 225 (1977); M. Kamimura, Nucl. Phys. A **351**, 456 (1981).
[5] Y. Funaki, A. Tohsaki, H. Horiuchi, P. Schuck, and G. Röpke, Phys. Rev. C **67**, 051306(R) (2003).
[6] N. Yamaguchi, S. Nagata, and J. Michiyama, Prog. Theor. Phys. **76**, 1289 (1986).
[7] H. O. Meyer, P. Schwandt, G. L. Moake, and P. P. Singh, Phys. Rev. C **23**, 616 (1981).
[8] J. R. Comfort and W. G. Love, Phys. Rev. C **26**, 1800 (1982).
[9] E. Sh. Sukhovitskii, S. Chiba, O. Iwamoto, and Y. V. Porodzinskii, Nucl. Phys. A **640**, 147 (1998).
[10] S. Kato, K. Okada, M. Kondo, K. Hosono, T. Saito, T. Matsuoka, K. Hatanaka, T. Noro, S. Nagamachi, H. Shimizu, K. Oginio, Y. Kadota, S. Matsuki, and M. Wakai, Phys. Rev. C **31**, 1616 (1985).
[11] T. Nojiri, M. Kamimura, and M. Sano, Prog. Theor. Phys. **66**, 1906 (1981).
[12] G. Bertsch, J. Borysowicz, H. Macmanus, and W. G. Love, Nucl. Phys. A **284**, 399 (1977).
[13] G. R. Satchler and W. G. Love, Phys. Rep. **55**, 183 (1979).
[14] M. E. Brandan and G. R. Sarchler, Phys. Rep. **285**, 143 (1997).
[15] Y. Hirabayashi, Y. Sakuragi, and Y. Abe, Phys. Rev. Lett. **74**, 4141 (1995).
[16] S. Ohkubo and Y. Hirabayashi, Phys. Rev. C **70**, 041602(R) (2004).
[17] Sh. Hamada, Y. Hirabayashi, N. Burtebayev, and S. Ohkubo, Phys. Rev. C **87**, 024311 (2013).
[18] M. Ito, Y. Sakuragi, and Y. Hirabayashi, Eur. Phys. J. A **5**, 373 (1999).
[19] M. Ito, Y. Hirabayashi, and Y. Sakuragi, Phys. Rev. C **66**, 034307 (2002).
[20] M. Ito, Y. Sakuragi, and Y. Hirabayashi, Phys. Rev. C **63**, 064303 (2001).
[21] G. R. Satchler, in *Direct Nuclear Reaction* (Oxford University Press, Oxford, UK, 1983), p. 205.
[22] N. K. Glendenning, in *Direct Nuclear Reactions* (Academic Press, San Diego, CA, 1983), p. 45.
[23] M. Tomita, M. Iwasaki, R. Otani, and M. Ito, Phys. Rev. C **89**, 034619 (2014).
[24] M. Tomita, M. Iwasaki, R. Otani, and M. Ito, J. Phys.: Conf. Ser. **569**, 012022 (2014).
[25] K. Hosono, M. Kondo, T. Saito, N. Matsuoka, S. Nagamachi, T. Noro, H. Shimizu, S. Kato, K. Okada, K. Ogino, and Y. Kadota, Nucl. Phys. A **343**, 234 (1980).
[26] H. Ohmura, J. Kasagi, F. Kamimoto, S. Kubono, and K. Koyama, J. Phys. Soc. Jpn. **48**, 1812 (1980).
[27] F. A. Brieva and J. R. Rook, Nucl. Phys. A **291**, 206 (1978).
[28] S. Chiba *et al.*, Nucl. Phys. A **624**, 305 (1997).